

Multi-frame Super-resolution from Noisy Data

Kireeti Bodduna, Joachim Weickert, and Marcelo Cárdenas

Mathematical Image Analysis Group, Faculty of Mathematics and Computer Science,
Saarland University, 66041 Saarbrücken, Germany.
{bodduna,weickert,cardenas}@mia.uni-saarland.de

Abstract. Obtaining high resolution images from low resolution data with clipped noise is algorithmically challenging due to the ill-posed nature of the problem. So far such problems have hardly been tackled, and the few existing approaches use simplistic regularisers. We show the usefulness of two adaptive regularisers based on anisotropic diffusion ideas: Apart from evaluating the classical edge-enhancing anisotropic diffusion regulariser, we introduce a novel non-local one with one-sided differences and superior performance. It is termed sector diffusion. We combine it with all six variants of the classical super-resolution observational model that arise from permutations of its three operators for warping, blurring, and downsampling. Surprisingly, the evaluation in a practically relevant noisy scenario produces a different ranking than the one in the noise-free setting in our previous work (SSVM 2017).

Keywords: super-resolution · denoising · anisotropic diffusion · non-local methods · one-sided derivatives

1 Introduction

Super-resolution (SR) is an image processing technique designed to overcome the resolution limits of cameras. Generating a high resolution (HR) image from one single low resolution (LR) image is referred to as single-frame super-resolution [7, 15, 24]. In this work, we concentrate on multi-frame super-resolution, where information from multiple LR images is fused into a single HR image [4, 6, 8–10, 12–18, 25].

In bio-medical and bio-physical applications we encounter images that possess a significant amount of noise. Multi-frame super-resolution in the presence of noise is thus practically relevant and also a very challenging research field. Algorithms that are designed to solve this problem compute derivative information on noisy data which showcases the ill-posed nature of the problem. In view of these algorithmic challenges, it is not surprising that very little efforts have been put into obtaining high resolution images from noisy low resolution data.

Deep learning-based methods are less suitable for bio-physical applications like electron microscopic imaging due to three main reasons: Firstly, there is very little ground truth data available. Secondly, the raw noise type is not well understood, unlike normal cameras. Finally, this imaging pipeline employs a huge

amount of steps to obtain the final structure of the specimen under observation. After each one of these steps, the noise type changes. This makes deep-learning models that are specifically trained for a particular kind of noise, sub-optimal.

In the present paper we specifically aim at reconstructing a HR image from its LR versions that have been corrupted by additive white Gaussian noise (AWGN).

Formalisation of the Problem. For multi-frame super-resolution, we want to find a HR image \mathbf{u} of resolution $N_H = H_1 \times H_2$ from N low resolution images $\{\mathbf{f}_i\}_{i=1}^N$ of resolution $N_L = L_1 \times L_2$. The low resolution images are assumed to be degraded versions of the real world HR scene. The standard formulation of the relation between the high resolution scene and its LR realisations is [5]

$$\mathbf{f}_i = \mathbf{D}\mathbf{B}\mathbf{W}_i\mathbf{u} + \mathbf{e}_i. \quad (1)$$

In this observational model, we express the motion of the objects in the image using the warping operator \mathbf{W}_i (size: $N_H \times N_H$). The operator \mathbf{B} (size: $N_H \times N_H$) denotes the blur due to the point spread function of the camera. We represent the downsampling of the HR scene by the camera detector system using \mathbf{D} (size: $N_L \times N_H$). The vector \mathbf{e}_i depicts the noise (error) acquired due to the imaging system. The operators \mathbf{B} and \mathbf{D} do not have an index i as we assume the same camera conditions for all images.

The standard model (1), however, has a disadvantage: The operator \mathbf{W}_i acts on the high-resolution scene \mathbf{u} . Hence, the model assumes that we have motion information at the high-resolution scale. In practice, we just have the downsampled and blurred images \mathbf{f}_i at our disposal. Motion at high-resolution must be approximated by upsampling the one computed on a lower resolution. Thus, the following question arises: Can one improve the practical performance of the SR approach by permuting the order of the operators? The seminal work of Wang and Qi [19] and the paper by Bodduna and Weickert [1] made progress in this direction. In [1], the authors tried to evaluate the SR observational model in a noise-free scenario by studying the six different alternatives that arise from permutations of its three operators \mathbf{D} , \mathbf{B} and \mathbf{W}_i . This has led to improvements in terms of both quality and speed, the former of which was also observed in [19]. However, such an evaluation is missing for the practically relevant scenario with noisy images. Our paper will address this problem.

Moreover, there is a second problem: For super-resolution of noisy data, the ideal observational model in (1) should be stabilised with a regulariser. In most cases, this is done by embedding it into the following quadratic energy minimisation framework:

$$E(\mathbf{u}) = \frac{1}{2} \sum_{i=1}^N |\mathbf{D}\mathbf{B}\mathbf{W}_i\mathbf{u} - \mathbf{f}_i|^2 + \frac{1}{2} \alpha |\mathbf{A}\mathbf{u}|^2. \quad (2)$$

Here, \mathbf{A} is a discrete approximation of the continuous gradient operator, α is the regularisation constant, and $|\cdot|$ denotes the Euclidean norm. The first term is the data term that encapsulates the observational model. The second one serves as

smoothness term which eliminates noise. Minimising (2) by setting its gradient to zero gives

$$\sum_{i=1}^N \mathbf{W}_i^\top \mathbf{B}^\top \mathbf{D}^\top (\mathbf{D} \mathbf{B} \mathbf{W}_i \mathbf{u} - \mathbf{f}_i) - \alpha \mathbf{A}_{\text{HD}} \mathbf{u} = \mathbf{0}, \quad (3)$$

where $\mathbf{A}_{\text{HD}} = \mathbf{A}^\top \mathbf{A}$ is the discrete approximation of the continuous Laplacian operator. In this paper, we use a Gaussian blur kernel, such that \mathbf{B}^\top equals \mathbf{B} . We denote the upsampling and downsampling matrices by \mathbf{D}^\top and \mathbf{D} , respectively. The operator \mathbf{W}_i represents forward warping, while \mathbf{W}_i^\top encodes backward registration. The explicit gradient descent scheme with parameters τ (the time step size) and k_{max} (the number of iterations) to solve Equation (3) is given by

$$\mathbf{u}^{k+1} = \mathbf{u}^k + \tau \left(\alpha \mathbf{A}_{\text{HD}} \mathbf{u}^k - \sum_{i=1}^N \mathbf{W}_i^\top \mathbf{B}^\top \mathbf{D}^\top (\mathbf{D} \mathbf{B} \mathbf{W}_i \mathbf{u}^k - \mathbf{f}_i) \right). \quad (4)$$

In this evolution equation, \mathbf{A}_{HD} acts as the denoiser. However, such a noise elimination scheme uses a simple homogeneous diffusion process that also blurs important structures. As far as the usage of diffusion-based regularisers for super-resolution is concerned, only a few papers with simplistic models are available. Thus, it is highly desirable to introduce more advanced structure preserving regularisers. This is our second challenge.

Our Contribution. To address the first problem, we investigate the performance of all permutations of the standard observational model in an AWGN setting that is clipped to the dynamic range $[0, 255]$. This practically relevant noise model covers over- and under-exposed image acquisition conditions.

To incorporate structure-preserving regularisers, we start with replacing the homogeneous diffusion operator by the classical model of edge-enhancing anisotropic diffusion (EED) [21]. Although this model is around since a long time, its performance for super-resolution has not been examined so far. Moreover, we also introduce a more sophisticated non-local anisotropic model that offers better structure preservation and superior noise elimination than EED. We call it sector diffusion (SD). It differs from all other diffusion models by the fact that it is fully based on one-sided derivatives.

We first compare the denoising performance of EED and SD for real-world images with clipped-AWGN, before we embed them as regularisers in the SR framework. We deliberately do not evaluate popular denoising methods such as 3D block matching [3] and non-local Bayes [11]: Most of these techniques rely heavily on a correct noise model, which renders them inferior for clipped noise, in particular with large amplitudes.

Paper Structure. Our paper is organised as follows: We introduce our novel sector diffusion model in Section 2. Here, we also review various super-resolution

Table 1: **Left:** The seven SR observational models. **Right:** Parameter settings for optical flow calculation. We have two model parameters: α_{OF} (smoothness parameter) and σ_{OF} (Gaussian pre-smoothing). Numerical parameters are chosen as $\eta = 0.95$ (downsampling factor), $\eta_1 = 10$ (inner fixed point iterations), $\eta_2 = 10$ (outer fixed point iterations) and $\omega = 1.95$ (successive over-relaxation parameter).

Model	Equation	Dataset	σ_{OF}	α_{OF}
M1	$DBW_i u + e_i = f_i$	Text1	2.6	13.3
M2	$DW_i B u + e_i = f_i$	Text2	1.0	15.6
M3	$BDW_i u + e_i = f_i$	Text3	2.3	6.3
M4	$W_i DB u + e_i = f_i$	House1	3.8	13.5
M5	$BW_i D u + e_i = f_i$	House2	1.2	17.0
M6	$W_i BD u + e_i = f_i$	House3	2.7	16.5
M2.1	$B u + e_i = D^T W_i^T f_i$			

observational models and the EED-based image evolution equation. In Section 3, we present several denoising and SR reconstruction experiments along with some discussions. Finally, in Section 4 we conclude with a summary about robust multi-frame SR reconstruction as well as an outlook on future work.

2 Modeling and Theory

In this section, we first review the various possible permutations of the super-resolution observational model in (1). Afterwards, we introduce the different regularisation schemes utilised for both denoising and SR reconstruction purposes.

2.1 Super-resolution Observational Models

Table 1 shows the various permutations of the original observational model M1 [1]. While models M2-M6 depict the five other possible permutations, M2.1 represents a technique that is derived from M2. The motivation behind the modelling of M1-M6 is quality reasons. M2.1, on the other hand, is designed to exploit the precomputable nature of the term on the right hand side of the corresponding equation. Such a design is faster than any of the other models.

2.2 Edge-enhancing Diffusion

Edge-enhancing diffusion was proposed by Weickert [21] with the goal to enhance smoothing along edges while inhibiting it across them. To achieve this, one designs a diffusion tensor D with eigenvectors v_1 and v_2 that are parallel and perpendicular to a Gaussian smoothed image gradient. This is followed by setting the eigenvalue corresponding to the eigenvector perpendicular to the

gradient to one, indicating full flow. The eigenvalue corresponding to the eigenvector parallel to the gradient is determined by a diffusivity function. Using this idea, one can inhibit smoothing across edges. The following is the continuous mathematical formulation of the evolution of image u under EED:

$$\partial_t u = \operatorname{div}(D(\nabla u_\sigma) \nabla u), \quad (5)$$

$$D(\nabla u_\sigma) = g(|\nabla u_\sigma|^2) \cdot \mathbf{v}_1 \mathbf{v}_1^T + 1 \cdot \mathbf{v}_2 \mathbf{v}_2^T, \quad (6)$$

$$\mathbf{v}_1 \parallel \nabla u_\sigma, \quad |\mathbf{v}_1| = 1 \quad \text{and} \quad \mathbf{v}_2 \perp \nabla u_\sigma, \quad |\mathbf{v}_2| = 1. \quad (7)$$

Here, div is the 2D divergence operator and ∇u the spatial gradient. The Gaussian-smoothed image is u_σ . Computing the gradient on u_σ makes the diffusion process robust under the presence of noise. Both EED and SD evolution equations are initialised with the noisy image \mathbf{f} . Finally, the diffusivity function $g(x)$ is chosen as [22]

$$g(x) = 1 - \exp\left(\frac{-3.31488}{\left(\frac{x}{\lambda}\right)^8}\right). \quad (8)$$

Thus, by replacing the Laplacian \mathbf{A}_{HD} in (4) with the space discrete version \mathbf{A}_{EED} of the EED operator in (5), we arrive at the EED-based scheme for reconstructing the high resolution scene:

$$\mathbf{u}^{k+1} = \mathbf{u}^k + \tau \left(\alpha(\mathbf{A}_{\text{EED}}(\mathbf{u}^k)) - \sum_{i=1}^N \mathbf{W}_i^\top \mathbf{B}^\top \mathbf{D}^\top (\mathbf{D} \mathbf{B} \mathbf{W}_i \mathbf{u}^k - \mathbf{f}_L^i) \right). \quad (9)$$

The details regarding the discretisation of the EED operator can be found in [23].

2.3 Sector Diffusion

Continuous Model. Our goal is to design a diffusion method with a higher adaptation to image structures than previous anisotropic models such as EED. To this end, we start with Weickert's integration model from [20]:

$$\partial_t u(\mathbf{x}, t) = \frac{1}{\pi} \int_0^\pi \partial_\theta (g(\partial_\theta u_\sigma) \partial_\theta u) d\theta. \quad (10)$$

Here, ∂_θ stands for the directional derivative in the direction represented by angle θ , g is the diffusivity function and u_σ denotes a convolution of u with a Gaussian of standard deviation σ . This model considers each orientation separately and is thus capable of diffusing along edges, but not across them.

In order to improve its structure adaptation even further, we replace the directional derivatives by one-sided directional derivatives and integrate over $[0, 2\pi]$ instead of $[0, \pi]$:

$$\partial_t u(\mathbf{x}, t) = \frac{1}{2\pi} \int_0^{2\pi} \partial_\theta^+ (g(\partial_\theta^+ u_\sigma) \partial_\theta^+ u) d\theta. \quad (11)$$

Here, u_σ^θ represents a one-sided smoothing of u in the orientation given by the angle θ , and ∂_θ^+ denotes a one-sided derivative in the same orientation. In contrast to the usual Gaussian smoothing applied in (10), this one-sided smoothing allows the filter to distinguish two different derivatives for a given direction: One in the orientation of θ , and the other in the orientation of $\theta + \pi$. A formal definition of these concepts can be realised by considering the restriction of u to the corresponding ray starting at \mathbf{x} , in the orientation of each θ . Namely, for fixed \mathbf{x}, t, θ , we consider $u(h; \mathbf{x}, t) := u(\mathbf{x} + h(\cos(\theta), \sin(\theta))^T, t)$, for $h \in [0, \infty]$. Then, the one-sided directional derivative ∂_θ^+ is formally defined as

$$\partial_\theta^+ u := \lim_{h \rightarrow 0^+} \frac{u(h; \mathbf{x}, t) - u(\mathbf{x}, t)}{h}. \quad (12)$$

To our knowledge, diffusion filters that are explicitly based on one-sided directional derivatives have not been described in the literature so far.

In order to introduce a second alteration of model (10), we incorporate the concept of non-locality. This leads to

$$\partial_t u(\mathbf{x}, t) = \int_{B_{x,\rho}} J(|\mathbf{y} - \mathbf{x}|) g \left(\frac{u_\sigma(\mathbf{y}; \mathbf{y} - \mathbf{x}) - u_\sigma(\mathbf{x}; \mathbf{y} - \mathbf{x})}{|\mathbf{y} - \mathbf{x}|} \right) (u(\mathbf{y}) - u(\mathbf{x})) d\mathbf{y}.$$

Here, $B_{x,\rho}$ denotes the disc with center x and radius ρ . The diffusivity g has already been defined in (8). Also, the function $J(s)$ is a slightly Gaussian-smoothed version of $F(s) := \frac{1}{s^2}$. Moreover, we assume that it decreases fast but smoothly to zero such that $J(s) = 0$ for $|s| \geq \rho$. The slight Gaussian smoothing of F is required for avoiding the singularity of J as $s \rightarrow 0$. The value $u_\sigma(\mathbf{z}; \mathbf{y} - \mathbf{x})$ corresponds to a one-dimensional Gaussian smoothing of u inside the segment $\lambda_{\mathbf{x}\mathbf{y}}(s) := \left\{ \mathbf{x} + s \frac{(\mathbf{y} - \mathbf{x})}{|\mathbf{y} - \mathbf{x}|} : s \in [0, \rho] \right\}$ evaluated at \mathbf{z} . This idea of making the diffusivity dependent on values inside an orientation dependent segment determines the structure preservation capabilities of the model. In the next paragraph we will see how to translate this non-local filter into a space-discrete version by dividing the disc $B_{x,\rho}$ into sectors. This explains the name *sector diffusion*.

Discrete Model. In order to properly adapt our filter to the local image structure, we first divide a disc shaped neighborhood $B_{i,\rho}$ of radius ρ centered around pixel i , into M sectors. With the objective of reducing interactions between regions of dissimilar grey values we employ robust smoothing within these sectors. This mirrors the continuous modelling idea of smoothing within the segments $\lambda_{\mathbf{x}\mathbf{y}}$. The final design objective is that we employ one-sided finite differences instead of central differences for discretisation purposes. The latter have a property of smoothing over the central pixel, thus destroying image structures. This idea is again a direct consequence of considering orientations rather than directions, in the continuous model. With these motivations in mind, we define the space-discrete formulation of the sector diffusion model as

$$\frac{du_i}{dt} = \mathbf{A}_{\text{SD}}(u) = \sum_{\ell=1}^M \sum_{j \in S_\ell} g_{i,j} \cdot \frac{u_j - u_i}{|\mathbf{x}_j - \mathbf{x}_i|^2}. \quad (13)$$

Table 2: MSE values of denoised images including parameters used. L40 stands for Lena image with $\sigma_{\text{noise}} = 40$. B, H, P denote Bridge, House and Peppers respectively.

Image	EED				SD			
	σ	λ	k_{\max}	MSE	σ	λ	k_{\max}	MSE
L40	1.2	7.5	34	98.67	0.6	3.1	7	92.99
L60	1.8	5.0	63	156.24	0.6	3.3	11	138.48
L80	2.0	4.6	87	230.28	0.6	2.9	18	180.66
B40	0.9	14.4	12	294.32	0.5	3.3	4	261.62
B60	1.1	13.4	20	418.71	0.5	4.1	6	360.87
B80	1.4	10.4	28	514.23	0.6	4.0	9	436.60
H40	0.9	11.1	34	96.62	0.7	2.6	9	104.31
H60	1.1	12.1	33	167.72	0.7	2.7	14	152.24
H80	1.8	5.8	72	247.09	0.6	2.7	19	207.65
P40	1.2	8.1	28	102.97	0.6	2.1	10	86.57
P60	1.7	5.6	51	200.31	0.6	1.8	19	133.19
P80	1.9	5.1	68	353.61	0.6	1.7	30	188.86

Here, $g_{i,j} = g\left(\frac{u_{\sigma j\ell} - u_{\sigma i\ell}}{|\mathbf{x}_j - \mathbf{x}_i|}\right)$, S_ℓ is the set of pixels within a particular sector ℓ , and \mathbf{x}_i and \mathbf{x}_j denote the position of the pixels i and j in the image grid. The sector-restricted smoothing is defined as

$$u_{\sigma j\ell} = \frac{1}{c} \sum_{k \in S_\ell} h(k, j, \sigma) u_k. \quad (14)$$

Here, c is a normalisation constant and

$$h(k, j, \sigma) = \exp\left(\frac{-|\mathbf{x}_k - \mathbf{x}_j|^2}{2\sigma^2}\right). \quad (15)$$

Similar to EED, we can now define the SD-based SR framework as

$$\mathbf{u}^{k+1} = \mathbf{u}^k + \tau \left(\alpha(\mathbf{A}_{\text{SD}}(\mathbf{u}^k)) - \sum_{i=1}^N \mathbf{W}_i^\top \mathbf{B}^\top \mathbf{D}^\top (\mathbf{D} \mathbf{B} \mathbf{W}_i \mathbf{u}^k - \mathbf{f}_L^i) \right). \quad (16)$$

3 Experiments and Discussion

In this section, we first evaluate EED and SD in terms of their denoising as well as SR regularisation capability. Then we choose the best of the two as regulariser for evaluating the operator orders in the SR observational model.

3.1 Denoising Experiments

Datasets. The test images for denoising experiments Lena, House, Peppers and Bridge¹ were corrupted with clipped-AWGN ($\sigma_{\text{noise}} = 40, 60$ and 80).

¹ <http://sipi.usc.edu/database/>

Table 3: MSE values of SR reconstructed images including parameters used. T2 stands for Text2 dataset with ground truth optical flow, while T2-S was computed using sub-optimal calculated flow. Ground truth image size for Text: 512×512 . T1-T3 represent images downsized by factors 1, 2 and 3, respectively. Image size for House: 256×256 . H1-H3 represent images downsized by factors 1, 1.5 and 2, respectively. Every dataset has 30 images each, with the last of them being the reference frame for registration.

Dataset	EED						SD					
	σ	σ_B	λ	α	k_{\max}	MSE	σ	σ_B	λ	α	k_{\max}	MSE
H1	0.6	0.8	11.0	118.0	37	110.45	0.9	1.0	2.0	1.6	17	83.12
H2	0.7	0.5	12.0	120.0	9	162.64	0.8	0.7	1.7	5.3	17	133.35
H2-S	0.7	0.5	13.0	115.0	9	172.94	0.9	0.8	1.8	4.5	17	141.62
H3	0.6	0.4	14.0	127.0	48	201.91	0.6	0.8	2.3	2.9	49	161.26
T1	1.0	1.1	9.0	14.0	136	164.72	0.6	1.1	3.0	0.3	48	158.50
T2	1.3	0.9	7.0	18.0	11	397.09	0.6	1.0	2.7	0.6	34	378.72
T2-S	1.3	1.0	7.0	18.0	14	510.80	0.6	1.1	2.9	0.5	32	499.60
T3	1.2	0.4	7.0	14.0	13	674.65	0.6	0.6	2.3	0.6	49	657.82

Table 4: Data term evaluation. **Left:** Text2 with ground truth flow. **Right:** Text2 with sub-optimal flow.

Model	σ	σ_B	λ	α	k_{\max}	MSE	Model	σ	σ_B	λ	α	k_{\max}	MSE
1	0.6	1.0	2.7	0.6	34	378.72	1	0.6	1.1	2.9	0.5	32	499.60
2	0.6	1.0	2.7	0.6	34	382.63	2	0.6	1.1	3.4	0.4	33	502.78
3	0.6	0.6	2.9	1.2	20	381.75	3	0.3	0.8	3.8	1.0	21	500.50
4	0.6	0.8	2.8	0.6	35	392.66	4	0.6	0.9	3.0	0.5	32	511.09
5	0.6	0.5	2.7	0.7	33	391.91	5	0.4	0.6	4.6	0.3	43	513.29
6	0.3	0.5	4.1	0.4	60	403.50	6	0.4	0.6	4.6	0.3	48	518.04
2.1	0.6	1.5	3.3	0.2	55	394.85	2.1	0.6	1.6	3.5	0.2	56	523.34

Parameter Selection. Our experience indicates that 36 sectors gives a reasonable directional resolution. Also, we have chosen the radius of the disc-shaped neighborhood to be 7 pixels. The time step size of the explicit scheme for SD was chosen such that the maximum–minimum principle is not violated. Our grid size is set to 1. For EED, we choose the time step size $\tau = 0.2$. All other parameters (Gaussian smoothing σ , diffusivity parameter λ , and number of iterations k_{\max}) have been optimised with respect to the mean squared error (MSE).

Denosing Performance. In the first experiment, using equations (5) and (13), we evaluate the denosing performance of EED and SD, respectively. It is clear from MSE values in Table 2 that SD produces better results. The superior performance of SD compared to EED can be attributed to its higher adaptivity towards image structures like edges.

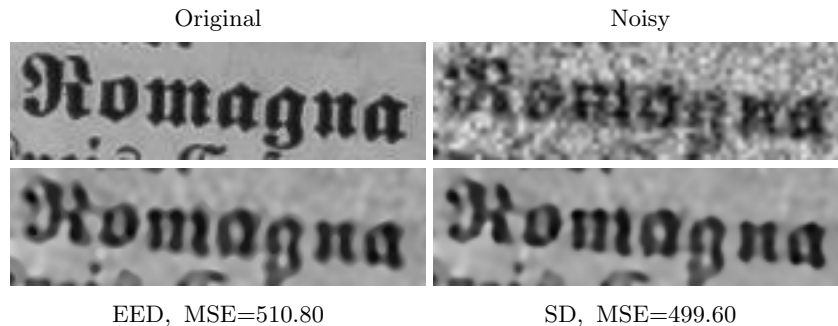


Fig. 1: Zoom into SR reconstructions for the Text2 dataset with sub-optimal flow.

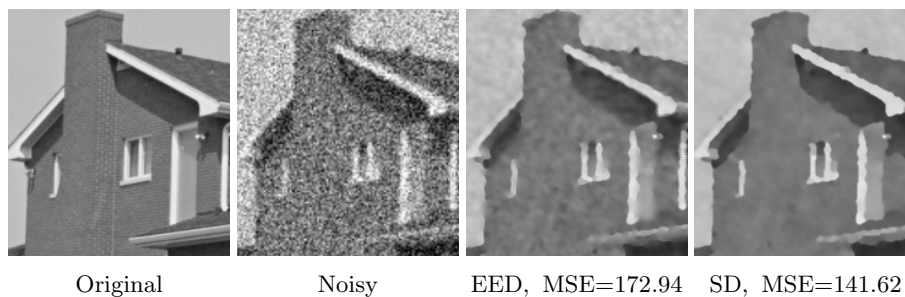


Fig. 2: Zoom into SR reconstructions for the House2 dataset with sub-optimal flow.

3.2 Super-resolution Reconstruction Experiments

Datasets. For the SR reconstruction experiments, we have considered two high-resolution scenes in the form of ‘Text’² and ‘House’ images. The ground truth HR images have been warped (randomly generated deformation motion), blurred (Gaussian blur with standard deviation 1.0), downsampled (with bilinear interpolation), and degraded by noise (clipped-AWGN with $\sigma_{\text{noise}}=40$).

Parameter Selection. To account for a large spectrum of optical flow qualities, we have used both the ground truth flow as well as a simplified approach of Brox et al. [2] without gradient constancy assumption. The parameters for different datasets are shown in Table 1. We optimise these parameters just once, but not after every super-resolution iteration. For SR reconstruction, we additionally optimise the parameters α (smoothness) and σ_B (Gaussian blur operator) apart from the already mentioned denoising parameters. Again the grid size is 1. As time step we choose $\tau = 0.05$ for EED and $\tau = 0.012$ for SD, giving experimental stability and convergence to a plausible reconstruction. We initialise \mathbf{u} with a bilinearly upsampled image.

² <https://pixabay.com/en/knowledge-book-library-glasses-1052014/>

Smoothness Term Evaluation. The SR reconstruction quality of the two regularisers is evaluated using equations (9) and (16). From Table 3 and Figures 1,2 we observe that SD outperforms EED consistently. This holds both for ground truth and suboptimal optical flow, over all downsampling factors.

Data Term Evaluation. Since we have observed a superior performance of SD for regularisation purposes, we also use it in the smoothness term while evaluating the data term with the observational model. Table 4 shows the MSE values of the reconstructed high resolution scene with all observational models from Table 1.

For ground truth flow, the observational model M1 performs best. This is in accordance with [1, 19]. For suboptimal flow, M1 also outperforms M2. Interestingly, this is in contrast to the findings in [1, 19], where M2 gave superior results for SR problems without noise. We explain this by the fact that we first warp the HR scene in M1. This introduces an error by applying a motion field computed from blurred LR images to sharp HR images. On the other hand, such an error does not occur for M2, as we first blur the HR scene. However, swapping blur and warp operators induces errors since matrix multiplication is not commutative. The error magnitude depends on the images and their noise. In our case, we conjecture that the latter error is higher than the former. Therefore, M1 outperforms M2.

In [1], model M2.1 was much faster than M2 with only little loss in reconstruction quality. However, this model becomes irrelevant in the noisy scenario, as M1 outperforms M2, and we also encounter a further quality loss when replacing M2 by M2.1.

4 Conclusion and Outlook

Our paper belongs to the scarce amount of literature that ventures to investigate super-resolution models in the practically relevant scenario of substantial amounts of clipped noise. In contrast to classical least squares approaches with homogeneous diffusion regularisation we have paid specific attention to structure preserving regularisers such as edge-enhancing anisotropic diffusion (EED). Interestingly, EED has not been used for super-resolution before, in spite of the fact that alternatives such as BM3D and NLB are less suited for super-resolution from data with clipped noise. More importantly, we have also proposed a novel anisotropic diffusion model called sector diffusion. It is the first diffusion method that consequently uses only one-sided directional derivatives. In its local formulation, this is a model that offers also structural novelties from a mathematical perspective, since it cannot be described in terms of a partial differential equation. From a practical perspective, the non-local sector diffusion possesses a higher structural adaptivity and a better denoising performance than simpler diffusion models. Thus, it appears promising to study its usefulness also in applications beyond super-resolution. This is part of our ongoing work.

Acknowledgements. J.W. has received funding from the European Research Council (ERC) under the European Union’s Horizon 2020 research and innovation programme (grant no. 741215, ERC Advanced Grant INCOVID). We thank our colleagues Dr. Matthias Augustin and Dr. Pascal Peter for useful comments on a draft version of the paper.

References

1. Bodduna, K., Weickert, J.: Evaluating data terms for variational multi-frame super-resolution. In: Lauze, F., Dong, Y., Dahl, A. (eds.) *Scale Space and Variational Methods in Computer Vision*. Lecture Notes in Computer Science, vol. 10302, pp. 590–601. Springer, Berlin (Jun 2017)
2. Brox, T., Bruhn, A., Papenberg, N., Weickert, J.: High accuracy optical flow estimation based on a theory for warping. In: Pajdla, T., Matas, J. (eds.) *Computer Vision – ECCV 2004, Part IV*, Lecture Notes in Computer Science, vol. 3024, pp. 25–36. Springer, Berlin (2004)
3. Dabov, K., Foi, A., Katkovnik, V., Egiazarian, K.: Image denoising by sparse 3D transform-domain collaborative filtering. *IEEE Transactions on Image Processing* **16**(8), 2080–2095 (Aug 2007)
4. Doulamis, A., Doulamis, N., Ioannidis, C., Chrysouli, C., Grammalidis, N., Dimitropoulos, K., Ptsiou, C., Stathopoulou, E., Ioannides, M.: 5d modelling: An efficient approach for creating spatiotemporal predictive 3d maps of large-scale cultural resources. *ISPRS Annals of the Photogrammetry, Remote Sensing and Spatial Information Sciences* **2**(5), 61–68 (Jan 2015)
5. Elad, M., Feuer, A.: Restoration of a single superresolution image from several blurred, noisy, and undersampled measured images. *IEEE Transactions on Image Processing* **6**(12), 1646–1658 (Dec 1997)
6. Farsiu, S., Robinson, M.D., Elad, M., Milanfar, P.: Fast and robust multi-frame super resolution. *IEEE Transactions on Image Processing* **13**(10), 1327–1364 (Oct 2004)
7. Glasner, D., Shai, B., Irani, M.: Super-resolution from a single image. In: *Proc. IEEE International Conference on Computer Vision (ICCV)*. pp. 349–356. Kyoto, Japan (Sep 2009)
8. Knoll, F., Bredies, K., Pock, T., Stollberger, R.: Second-order total generalized variation (TGV) for MRI. *Magnetic Resonance in Medicine* **65**(2), 480–491 (Feb 2011)
9. Kosmopoulos, D., Doulamis, N., Voulodimos, A.: Bayesian filter based behavior recognition in workflows allowing for user feedback. *Computer Vision and Image Understanding* **116**, 422–434 (Mar 2012)
10. Laghrib, A., Hakim, A., Raghay, S.: A combined total variation and bilateral filter approach for image robust super resolution. *EURASIP Journal on Image and Video Processing* **2015**(1), 19 (June 2015)
11. Lebrun, M., Buades, A., Morel, J.: A nonlocal Bayesian image denoising algorithm. *SIAM Journal on Imaging Sciences* **6**(3), 1665–1688 (Sep 2013)
12. Li, X., Mooney, P., Zheng, S., Booth, C., Braunfeld, M., Gubbens, S., Agard, D., Cheng, Y.: Electron counting and beam-induced motion correction enable near-atomic-resolution single-particle cryo-EM. *Nature Methods* **10**(6), 584–590 (Jun 2013)

13. Lin, F., Fookes, C., Chandran, V., Sridharan, S.: Investigation into optical flow super-resolution for surveillance applications. In: Lovell, B.C., Maeder, A.J. (eds.) *APRS Workshop on Digital Image Computing: Pattern Recognition and Imaging for Medical Applications*. pp. 73–78. Brisbane (Feb 2005)
14. Makantasis, K., Karantzas, K., Doulamis, A., Doulamis, N.: Deep supervised learning for hyperspectral data classification through convolutional neural networks. In: *Proc. IEEE International Geoscience and Remote Sensing Symposium (IGARSS)*. pp. 4959–4962 (Jul 2015)
15. Marquina, A., Osher, S.: Image super-resolution by TV-regularization and Bregman iteration. *Journal of Scientific Computing* **37**(3), 367–382 (Dec 2008)
16. Pham, T., Vliet, L., Schutte, K.: Robust fusion of irregularly sampled data using adaptive normalized convolution. *EURASIP Journal on Advances in Signal Processing* **2006**(083268) (Dec 2006)
17. Tatem, A., Lewis, H., Atkinson, P., Nixon, M.: Super-resolution target identification from remotely sensed images using a Hopfield neural network. *IEEE Transactions on Geoscience and Remote Sensing* **39**(4), 781–796 (Apr 2001)
18. Tatem, A., Lewis, H., Atkinson, P., Nixon, M.: Super-resolution land cover pattern prediction using a Hopfield neural network. *Remote Sensing of Environment* **79**(1), 1–14 (Jan 2002)
19. Wang, Z., Qi, F.: On ambiguities in super-resolution modeling. *IEEE Signal Processing Letters* **11**(8), 678–681 (Aug 2004)
20. Weickert, J.: Anisotropic diffusion filters for image processing based quality control. In: Fasano, A., Primicerio, M. (eds.) *Proc. Seventh European Conference on Mathematics in Industry*, pp. 355–362. Teubner, Stuttgart (1994)
21. Weickert, J.: Theoretical foundations of anisotropic diffusion in image processing. In: Kropatsch, W., Klette, R., Solina, F., Albrecht, R. (eds.) *Theoretical Foundations of Computer Vision, Computing Supplement*, vol. 11, pp. 221–236. Springer, Vienna (1996)
22. Weickert, J.: *Anisotropic Diffusion in Image Processing*. Teubner, Stuttgart (1998)
23. Weickert, J., Welk, M., Wickert, M.: L2-stable nonstandard finite differences for anisotropic diffusion. In: Kuijper, A., Bredies, K., Pock, T., Bischof, H. (eds.) *Scale Space and Variational Methods in Computer Vision*. pp. 380–391. *Lecture Notes in Computer Science*, Springer, Berlin (Jun 2013)
24. Yang, J., Wright, J., Huang, T., Ma, Y.: Image super-resolution via sparse representation. *IEEE Transactions on Image Processing* **19**(11), 2681–2873 (May 2010)
25. Yuan, Q., Zhang, L., Shen, H.: Multiframe super-resolution employing a spatially weighted total variation model. *IEEE Transactions on Circuits, Systems and Video Technology* **22**(3), 379–392 (Mar 2012)